Self-Guiding of Long-Wave Infrared Laser Pulses Mediated by Avalanche Ionization

D. Woodbury,[1] A. Goffin,[1] R. M. Schwartz,[1] J. Isaacs,[2] and H. M. Milchberg[1,*]
[1]Institute for Research in Electronics and Applied Physics, University of Maryland, College Park, Maryland 20742, USA
[2]Plasma Physics Division, U.S. Naval Research Laboratory, 4555 Overlook Avenue SW, Washington, DC 20375, USA

(Received 16 March 2020; revised 18 August 2020; accepted 24 August 2020; published 21 September 2020)

Nonlinear self-guided propagation of intense long-wave infrared (LWIR) laser pulses is of significant recent interest, as it promises high power transmission without beam breakup and multifilamentation. Central to self-guiding is the mechanism for the arrest of self-focusing collapse. Here, we show that discrete avalanche sites centered on submicron aerosols can arrest self-focusing, providing a new mechanism for self-guided propagation of moderate intensity LWIR pulses in outdoor environments. Our conclusions are supported by simulations of LWIR pulse propagation using an effective index approach that incorporates the time-resolved plasma dynamics of discrete avalanche breakdown sites.

DOI: 10.1103/PhysRevLett.125.133201

Femtosecond filamentation in gases and condensed media arises when nonlinear self-focusing of a high power laser pulse overcomes diffraction, with self-focusing rapidly increasing until it becomes self-limiting (pulse collapse arrest). The dynamic interplay of self-focusing, collapse arrest, and diffraction enables self-guided propagation of high-intensity beams (filaments) over extended distances [1]. Pulse collapse occurs for pulses whose peak power P exceeds a critical value $P_{cr} = 3.77\lambda^2/8\pi n_0 n_2$ for Gaussian beams, where λ is the laser wavelength, and n_0 and n_2 are the medium's linear and nonlinear indices of refraction. For ultrashort ($< \sim 100$ fs) near-IR pulses in air with $P \gtrsim P_{cr}$, self-focusing (from electronic and rotational nonlinearities in N_2 and O_2 [2]) continues until multiphoton or tunneling ionization of air molecules arrests the collapse via plasma defocusing, leading to $\sim$100 μm diameter high-intensity filaments. As input power is increased well beyond P_{cr}, the beam breaks up into multiple filaments, limiting the peak power delivered in a single high-intensity channel. The $P_{cr} \propto \lambda^2$ scaling gives higher beam breakup thresholds for longer wavelengths, stimulating recent interest in mid-IR and long-wave IR (LWIR) filamentation [3–12]. In addition, for LWIR pulses, new collapse arrest mechanisms have been proposed, including carrier-wave steepening and harmonic walk-off for short ($<$1 ps) pulses [3–10] and avalanche ionization seeded by many-body-induced ionization for longer ($>$1 ps) pulses [11–13]. A recent high sensitivity experiment [14], however, has shown that many-body ionization in atmospheric density gases is undetectable, leaving recent observations of self-guiding of $\sim$3 ps LWIR pulses [12] unexplained.

In this Letter, we describe and simulate a new self-guiding mechanism in the LWIR based on aerosol-seeded avalanche ionization at discrete breakdown sites. This mechanism appears essential for atmospheric self-guiding of moderate intensity LWIR pulses in outdoor conditions. In the absence of aerosols, we find that air avalanche is insufficient to prevent premature pulse collapse to narrow beams, even when including the contaminants measured in our prior experiments [14]. Aerosols, on the other hand, lead to enhanced, *saturable* ionization early in the pulse, enabling avalanche-mediated collapse arrest and self-guiding of few picosecond LWIR pulses at moderate intensity in wider beams, consistent with recent experiments [12]. Our results are qualitatively summarized in Fig. 1, which depicts simulations (to be explained below) of $\sim$1 TW/cm^2, 3.5 ps, $w_0 = 4$ mm LWIR pulses at $\lambda = 10.2$ μm propagating in air with and without aerosols

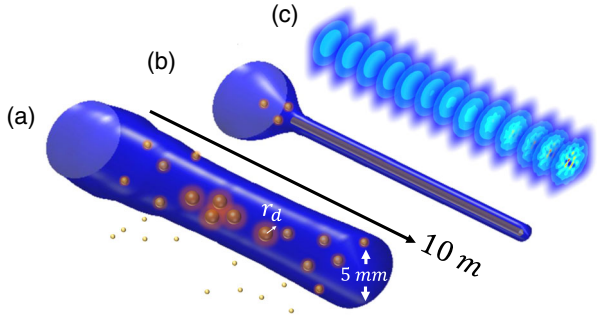

FIG. 1. Comparative propagation simulations [15] for initial 1 TW/cm^2, $w_0 = 4$ mm ($1/e^2$ intensity radius), 3.5 ps pulses. (a) $\lambda = 10.2$ μm LWIR pulse. Aerosols (yellow balls) seed rapid discrete avalanche breakdowns of characteristic size r_d, which arrest the collapse of a high power pulse, leading to a wide self-guided channel. (b) $\lambda = 10.2$ μm LWIR pulse. Here, in aerosol free air, avalanche breakdown initiated by single electrons from tunneling ionization proceeds too slowly to arrest collapse; collapse is arrested by continuous plasma formation and harmonic walk-off, leading to a smaller, high-intensity channel. This is not what is observed in experiments [12]. (c) $\lambda = 0.8$ μm near-IR pulse. Beam slices show filamentation and beam breakup.

present [(a) and (b)], showing that under these conditions aerosol plasmas are essential to arrest pulse collapse, leading to wide diameter self-guided beams. Illustrating the advantages of LWIR, Fig. 1(c) shows a simulation for a near-IR pulse ($\lambda = 0.8$ μm, $w_0 = 4$ mm, 3.5 ps), also at $\sim$1 TW/cm^2, where the pulse collapses and splinters into multiple narrow filaments.

We first review our new simulation framework, which includes a method for including discrete, transient breakdown sites in a high-intensity laser propagation simulation, and an improved avalanche model, incorporating the latest understanding of LWIR ionization processes in air provided by our recent experiments [14,28,29].

To proceed, we first consider how avalanche breakdown at discrete sites in a background gas [14,28,29] affects laser propagation. In avalanche breakdown, a free electron undergoes laser-driven dephasing elastic collisions with neutral molecules until it has enough kinetic energy to collisionally ionize them. The resulting growth in the local number of electrons at an avalanche site is exponential, $n_e = n_{eo}e^{\nu_i t}$, where $\nu_i = \langle\sigma_i v\rangle N_n$ is the electron collisional growth rate, n_{eo} is the local number of initial electrons (seeds), N_n is the local neutral molecule density, and $\langle\sigma_i v\rangle = \int_0^\infty dv\, f(v)\sigma_i(v)v$ for electron velocity distribution $f(v)$ and collisional ionization cross section σ_i. Growth saturates as the neutral density is depleted ($N_n = N_{no} - N_e$) for increasing electron density N_e.

A typical breakdown site plasma radius is limited by diffusion to $r_d \sim \sqrt{2\tau k_B T_e/m_e\nu_{en}} = 0.3\sqrt{\tau[\text{ps}]T_e[\text{eV}]}$ μm for electron temperature T_e and electron-neutral collision rate $\nu_{en} \sim 2$–4 ps^{-1} [30,31]. This gives $r_d \sim 5$ μm even for $k_B T_e \sim 100$ eV for a <3.5 ps pulse, a baseline size we use in our propagation simulations below. The laser will not interact with a continuous plasma unless the seed electron density satisfies $N_{e0} > 1/r_d^3 \sim 10^9$–$10^{11}$ cm^{-3}. The distribution of such diffusion-limited breakdown sites relative to a laser beam is shown schematically in Fig. 1.

In general, the effect of such discrete scatterers on laser propagation occurs through forward Mie scattering [32], and also requires 3D simulation of propagation through randomly distributed scatterers. Under our conditions, however, significant simplification is possible. As shown in [32], scattering from randomly distributed scattering sites of uniform size leads to an effective *continuum* refractive index provided there are many scatterers within a characteristic propagation volume. Here, if we consider this volume to be the cross sectional area of the beam multiplied by one-tenth of the Rayleigh length, or $V_p \sim \pi^2 w_0^4/10\lambda$ for beam waist w_0, then the propagation volume is on the order of $\sim$1 cm^3 even for $w_0 \sim 1$ mm, and $N_{sc}V_p \gg 1\times$ if the number density of scatterers $N_{sc} \gg 1$ cm^{-3}, a condition satisfied throughout this Letter. Further, we note that the changes in refractive index and laser propagation phase across an individual breakdown site of radius a, $|\Delta n| = |n-1| \sim \overline{N_e}/2N_{cr}$ and $|\Delta\Phi| = 4\pi a|\Delta n|/\lambda$, are both are small ($\ll$1) for site average plasma density well below critical density, $\overline{N_e} \ll N_{cr} = 1.1\times 10^{21}$ cm$^{-3}/\lambda^2$ [μm]. Thus, scattering occurs in the so-called Rayleigh-Gans (RG) regime, (defined by $|\Delta n| \ll 1$ and $a \ll \lambda/|\Delta n|$ [32]). Closely following the approach of [32], we find that in the RG regime, a medium composed of an ensemble of avalanche breakdown sites has an effective index $n_{\text{eff}} = 1 + N_{sc}V\Delta n = 1 - N_{sc}V(\overline{N_e}/2N_{cr})$, for average breakdown site volume V (full derivation in [15]). This index is equivalent to that of a continuous plasma of density $N_{sc}V\overline{N_e}$, as covered in previous work on exploding nanoplasmas [33]. The RG approximation breaks down as $\overline{N_e}$ approaches N_{cr} at individual breakdown sites, necessitating Mie scattering calculations. This limits our use of RG-based n_{eff} to breakdowns with $\overline{N_e} < N_{cr}/2 \sim 5\times 10^{18}$ cm^{-3} (at $\lambda = 10.2$ μm), corresponding to $\sim 6\times 10^9$ electrons in a $a = r_d = 5$ μm breakdown volume, for which Mie calculations and the RG approach give effective refractive indices within 20% [15]. Above this density, our simulations have limited fidelity.

To couple the ensemble of discrete plasmas to a propagation simulation, we next need a model for laser-driven avalanche. The best, albeit forbidding, approach is to calculate ν_i by solving the Boltzmann equation for the full time-resolved laser-driven electron distribution function $f(v)$ [34–37], accounting for angle-resolved scattering over wide primary and secondary electron energy ranges. Instead, we improve upon a temperature-based model [38–40], briefly described here.

Free electrons in a laser field of intensity I have a cycle-averaged ponderomotive kinetic energy $U_p \cong 0.93I$ [TW/cm^2]$(\lambda[\mu\text{m}])^2$ eV, which through electron-neutral collisions at rate ν_{en} drive collisional heating at a rate per electron of $W_{\text{coll}} = 2U_p\nu_{en}(1+\nu_{en}^2/\omega^2)^{-1} \sim 2U_p\nu_{en}$ (for laser frequencies $\omega/\nu_{en} \gg 1$ at atmospheric pressure). Electron heating is offset by losses, including rovibrational and electronic excitation, dissociation and ionization losses of energy χ_l and excitation rate ν_l in N_2 and O_2 [30,31]. The rate of change in plasma internal energy density is then

$$\frac{dU}{dt} = \frac{3}{2}\frac{d(k_B N_e T)}{dt} = \frac{3}{2}k_B\left(\frac{dN_e}{dt}T + \frac{dT}{dt}N_e\right) = 2\nu_{en}N_e U_p + \nu_i N_e U_p - \sum_l N_e\nu_l\chi_l, \quad (1)$$

where k_B is Boltzmann's constant. In the present work, we have added the term $U_p(dN_e/dt) = \nu_i N_e U_p$ to account for the effective heating of electrons collisionally released during the laser cycle. We ignore diffusive losses for laser spot sizes much larger than r_d: temperature gradients are weak because ν_{en} greatly exceeds the electron-electron and electron-ion collision rates, with no spatial dependence until saturation at the end of the breakdown [15]. Rearranging gives

$$\frac{dk_BT}{dt} = \frac{2}{3}(2U_p\nu_{en} + \nu_i U_p - \Sigma_l \nu_l \chi_l) - \nu_i T, \qquad (2)$$

where $N_e^{-1}(dN_e/dt)T = \nu_i T$ tracks thermal energy redistribution in a growing electron population [38–40]. Here, to obtain ν_{en}, ν_i, and the ν_l, we directly integrated the relevant cross sections in N_2 and O_2 [30,31] over a Maxwellian distribution up to $k_BT = 1$ keV, rather than using low energy tabulated rates [38–41]. With these rates as a function of temperature, Eq. (2) is then coupled to our laser propagation model (see later).

To provide a physical scale for the rates applicable to our propagation regime of interest, in Fig. 2(a) we plot the heating and loss rates from Eq. (2), $(dk_BT/dt)_{\text{heating}} = 2U_p(2\nu_{en} + \nu_i)/3$ and $|(dk_BT/dt)_{\text{loss}}| = 2(\Sigma_l \nu_l \chi_l)/3 + \nu_i T$, vs temperature for a $\lambda = 10.2$ μm, 1 TW/cm^2 pulse. The right scale shows the ionization rate $\nu_i(k_BT)$ as a function of temperature and, for comparison, the rate $\nu_i(E)$

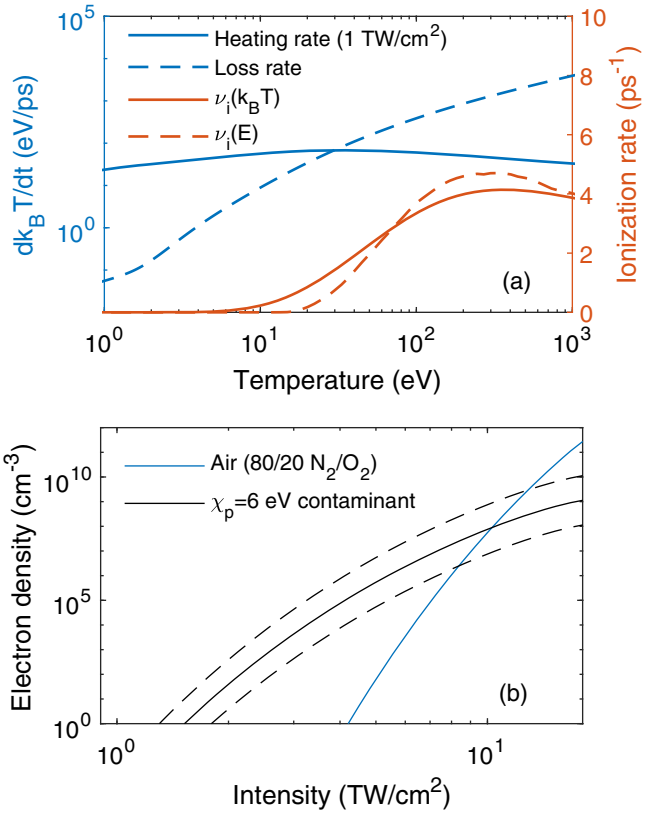

FIG. 2. (a) Temperature-dependent heating and loss rates $(dk_BT/dt)_{\text{heating}} = 2U_p(2\nu_{en} + \nu_i)/3$ (for $\lambda = 10.2$ μm, 1 TW/cm^2) and $|(dk_BT/dt)_{\text{loss}}| = 2(\Sigma_l \nu_l \chi_l)/3 + \nu_i T$ (left scale, log) in air. The corresponding ionization growth rate ν_i (right scale) is shown as a function of electron energy E and temperature T. (b) Generated electron density vs peak intensity from ionization of air and a $\chi_p \sim 6$ eV contaminant [14] by a $\lambda = 10.2$ μm, 1 ps FWHM Gaussian pulse. Dashed lines indicate bounds of approximate uncertainty in the number density of contaminant species [14].

for a monoenergetic electron distribution. Compared to a full Boltzmann treatment, the temperature-based approach of Eq. (2) greatly reduces the computational complexity, is insensitive to our assumption of a Maxwellian electron energy distribution, and captures the key physics. This is shown in the Supplemental Material [15] by comparing with experiments, full Boltzmann models, and limiting cases.

The initial free electron seeding of LWIR avalanche plays a crucial role in the details of collapse arrest. In aerosol-free air, free electrons are generated by tunneling and multiphoton ionization of N_2 and O_2, as shown in Fig. 2(b). In addition, we recently measured a ubiquitous air contaminant with ionization potential $\chi_p \sim 6$ eV at relative concentrations $\sim 10^{-9} - 10^{-11}$ (number density $10^8 - 10^{10}$ cm^{-3}) [14], which dominates ionization below ~ 10 TW/cm^2. Separately, aerosols (solid density particulates including dust, water droplets or fog, etc.) are readily ionized due to near-field enhancement or existing static charge. We recently estimated aerosol concentrations of $\sim 10^4$ cm^{-3} in our lab air by measuring the number of avalanches inside a breakdown threshold volume with and without particulate filtering [29]. Other detailed measurements of aerosols in indoor environments show a range of number concentration ($N_{\text{sc}} \sim 10^2 - 10^4$ cm^{-3}) and particle size ($\sim$0.1–10 μm) [42–44]. In general, aerosol concentrations are higher in outdoor "field" conditions envisioned for applications of self-guiding.

We can estimate the requirements for avalanche-mediated collapse arrest and self-guiding by equating the nonlinear index shifts associated with Kerr focusing and plasma refraction: $\Delta n_{\text{Kerr}} = \Delta n_{\text{eff}} \rightarrow n_2 I = N_{\text{sc}} V \overline{N_e}/2N_{\text{cr}}$. For $n_2 \sim 5 \times 10^{-19}$ cm$^2/W$ [45,46] and $V = 4\pi r_d^3/3$, we get $(N_{\text{sc}} V \overline{N_e}) \sim 10^{13} \times I\,[\text{TW/cm}^2]\,\text{cm}^{-3}$. At $I = 1$ TW/cm^2, one could have $N_{\text{sc}} \sim 10^4$ cm^{-3} breakdown sites avalanched to $\overline{N_e} \sim N_{\text{cr}}/2$, the limit of our effective index approximation. Alternatively, one could have a larger N_{sc} avalanched to a lower terminal $\overline{N_e}$.

Propagation simulations consisted of the avalanche model [$n_e = n_{eo} e^{\nu_i t}$ plus Eq. (2)] coupled to a 2D + time axisymmetric unidirectional pulse propagation equation (UPPE) solver [15,47,48]. To efficiently simulate multiple meters of propagation on our single GPU, we modified the UPPE algorithm by shifting the laser carrier frequency to zero, effectively calculating the envelope evolution. This reduces requirements on temporal resolution while maintaining dispersion, spectral broadening, and intensity-dependent effects, but neglects harmonic generation [15] and thus fails in situations where harmonic walk-off is dominant [9].

We now simulate a recent experiment observing long range self-guiding of a picosecond CO_2 laser pulse (3.5 J, 3.5 ps, $\lambda = 10.2$ μm, $P \sim 2P_{\text{cr}}$) initially focused to a 4 mm FWHM spot (4 TW/cm^2, $\sim$5 m Rayleigh range) in air [12]. The pulses initially self-focused and created a

tenuous visible plasma over ~5 m, followed by beam expansion to ~1 cm FWHM and self-guiding over ~30 m at peak intensities ~1 TW/cm^2, accompanied by pulse shortening to ~1.8 ps. Since generation of seed electrons from tunneling ionization of air is negligible at this intensity [Fig. 2(b)], the avalanche-generated plasma responsible for self-guiding was thought to be seeded by many-body induced ionization [11–13]. Our recent work [14] cast doubt on this seed source and suggested that the low level $\chi_p \sim 6$ eV contaminant might instead provide the necessary seed electrons. Below, we separately test the effect of this contaminant and of aerosols on LWIR pulse propagation.

We first consider air that includes the $\chi_p \sim 6$ eV contaminant but no aerosols, initializing propagation at the beam waist (4 mm FWHM, 4 TW/cm^2). Seed electrons were contributed by tunneling or multiphoton ionization [49] (see Fig. 2). Figure 3(a) shows the peak intensity and plasma density (at the peak intensity and after the pulse) versus propagation distance. The pulse self-focuses to ~20 TW/cm^2 after 2.25 m of propagation while also undergoing self-shortening to ~2 ps as the front and rear diffract [Fig. 3(b)]. At this point, substantial tunneling ionization occurs at the leading edge of the pulse, generating a seed electron density $N_{sc} \sim 10^{12}$ cm$^{-3} > r_d^{-3}$, in the continuous density regime. The falling edge of the pulse drives continued avalanche to high density, leading to further pulse shortening [Fig. 3(c)]. Beyond ~2.25 m, our shifted-carrier model breaks down; a separate carrier-resolved UPPE simulation shows that harmonic generation and walk-off [9,10] arrest pulse collapse, rather than plasma defocusing [15]. The final pulse continues to filament with peak intensity $I \sim 20$ TW/cm^2 and ~1 mm FWHM beam size [10,15], very different from the ~1 TW/cm^2, ~1 cm diameter self-guided beam observed in [12].

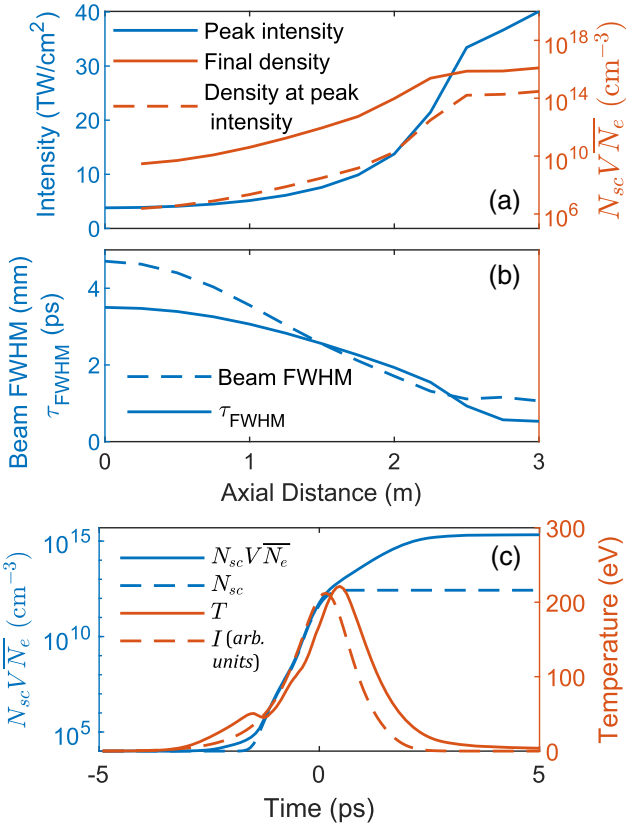

FIG. 3. (a),(b) Pulse parameters over 3 m of propagation. (a) Left axis, pulse peak intensity (TW/cm^2). Right axis, density at the intensity peak of the pulse (dashed) and after the pulse has completely passed (solid). (b) Beam FWHM and temporal FWHM. (c) On-axis intensity and plasma density and temperature after 2.25 m of propagation, showing a rapid increase in the density N_{sc} of breakdown sites due to seed generation by tunneling (dashed blue line), followed by slower increase in volume average density $N_e = N_{sc}V\overline{N_e}$ due to avalanche. Temperature (solid, right scale) roughly follows the pulse intensity profile (dashed).

The failure of avalanche in aerosol-free air to arrest collapse before the onset of tunneling is inevitable given the electron density growth rates in Fig. 2(a) and ionization yields in Fig. 2(b). Even for the maximum growth rate of $\nu_i = 4.7$ ps^{-1}, an initial electron density $N_{eo} \sim 10^9$ is needed to reach the effective density $N_{sc}V\overline{N_e} = 10^{13}$ cm^{-3} we estimated for self-guiding at 1 TW/cm^2. This initial density in turn requires tunneling at ~10 TW/cm^2 in the leading edge of the pulse as shown in Fig. 2, a conclusion unaffected by the presence of the $\chi_p \sim 6$ eV contaminant. Thus, it is unlikely that the ~1 TW/cm^2 channeling observed in [12] is stabilized by avalanche from electrons liberated by tunnel ionization.

Avalanche ionization in aerosols, however, introduces a new propagation regime consistent with self-guiding of modest intensity pulses. For the near-solid density of an aerosol particle, the electron-neutral collision rate ($\nu_{en} \sim 10^{15}$ s^{-1}) is much higher than infrared frequencies ($\omega/\nu_{en} \ll 1$) [35,50]. Thus collisional heating $W_{\rm coll} \propto I\nu_{en}^{-1}[1 + (\omega/\nu_{en})^2]^{-1} \approx I/\nu_{en}$ becomes wavelength independent for $\lambda \gtrsim 300$ nm, such that ionization rates calculated for breakdown in fused silica by $\lambda = 1$ μm pulses in Ref. [35] can be applied to the present simulation. Using these growth rates, we find a 3.5 ps, 1 TW/cm^2 pulse ionizes atoms in a ~0.2 μm radius particle in the far leading edge of the pulse, after accounting for field enhancement at the particle surface [15]. This plasma would then explode into the surrounding air and continue to avalanche. We assume the plasma is limited by diffusion to the same radial size ($r_d \sim 5$ μm) as for single electron seeds, and apply Eq. (2) to calculate further electron density growth.

Accordingly, we ran a second set of propagation simulations for a range of initial aerosol densities ($N_{sc} \sim 10^3 - 3 \times 10^4$ cm^{-3}), with results for $N_{sc} = 2 \times 10^4$ cm^{-3} shown in Fig. 4. For simplicity and specificity, we assumed a uniform aerosol radius of $a = 0.2$ μm.

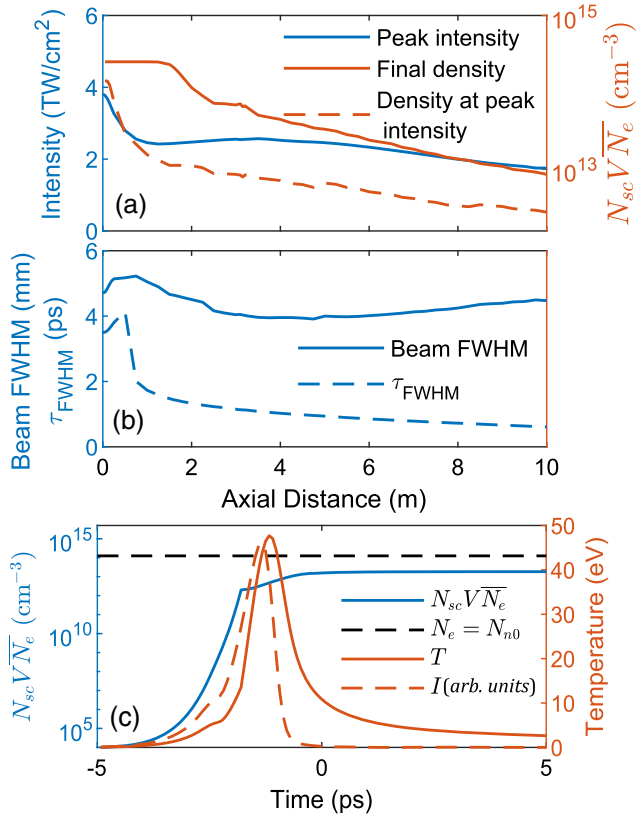

FIG. 4. (a),(b) Simulation parameters including aerosol-enhanced avalanche for initial aerosol density of 2×10^4 cm^{-3}. (c) On-axis intensity and plasma density and temperature after 6 m of propagation, showing a rapid increase in density due to breakdowns in aerosols, followed by slower avalanche in air, with volume average density reaching $\sim 10^{13}$ cm^{-3} near the intensity peak of the pulse, broadly consistent with self-guiding as shown above. The horizontal dashed line indicates the limit of full ionization of the aerosol-initiated breakdown sites. Right scale, distorted intensity profile (dashed) and corresponding plasma temperature (solid).

In these simulations, shown in Fig. 4, the pulse is immediately shortened as energy in the falling edge is scattered off-axis by the rapidly formed plasmas. After this transient, aerosol-enhanced plasma generation is sufficient to arrest self-focusing, resulting in self-guiding of 0.5–1.5 ps pulses at $\sim 2 - 2.5$ TW/cm^2 in a 4–5 mm spot over ~ 10 m, as seen in Figs. 4(a) and 4(b). Runs for lower aerosol densities ($N_{sc} < 10^4$ cm^{-3}) showed slower self-focusing, with collapse ultimately arrested by tunneling ionization [15], leading to behavior similar to Fig. 3.

Figure 4(c) shows the on-axis plasma density evolution and pulse shape at 6 m, well into self-guiding. In contrast to Fig. 3, the aerosols provide a rapid increase in $N_{sc}V\overline{N_e}$ that arrests collapse over the full pulse envelope, with ionization saturation limiting further pulse shortening. Thus, avalanche breakdown of aerosols appears essential for long distance stable self-guiding of moderate intensity picosecond LWIR pulses.

In summary, we have presented a new self-focusing collapse arrest mechanism leading to long range self-guiding of long wavelength infrared (LWIR) picosecond laser pulses in the atmosphere: an ensemble of transient avalanche breakdown sites centered on aerosols. In aerosol-free air, avalanche ionization seeded by tunneling is insufficient to arrest pulse collapse before high intensities and narrow filaments are reached; at sufficient laser power, this process would lead to multifilamentation and beam breakup. By contrast, aerosol-centered avalanche sites enhance plasma generation and enable long range self-guiding at moderate intensities with large channel diameters, consistent with recent experiments [12].

While our simulations have made a complex problem tractable and provided a clear physical picture for the role of aerosols, our work calls for more detailed studies. In particular, because local density can reach $\overline{N_e} \geq N_{cr}/2$ at breakdown sites during the pulse, and because the saturated aerosol plasma can further heat and expand into the background air, the RG model breaks down and would need to be replaced by full Mie scattering computations coupled to plasma dynamics. This plasma growth to larger discrete breakdowns could reduce the necessary aerosol concentration to $10^2 - 10^3$cm^{-3}. A full carrier frequency-resolved propagation simulation could also determine whether harmonic walk-off [9,10] reduces the aerosol concentration needed for collapse arrest. Future experimental propagation studies of picosecond LWIR pulses in controlled atmospheres will help further quantify these effects.

The authors thank P. Sprangle, M. Kolesik, J. Moloney, S. Tochitsky, and C. Joshi for useful discussions, J. Griff-McMahon for help with the simulations, and J. K. Wahlstrand for help calculating tunneling ionization rates. This work is supported by the Office of Naval Research (ONR) (N00014-17-1-2705, N00014-20-1-2233) and the Air Force Office of Scientific Research (AFOSR) (FA9550-16-1-0121, FA9550-16-1-0284). D. W. acknowledges support from the DOE NNSA SSGF program under DE-NA0003864.

*Corresponding author.
milch@umd.edu

[1] A. Couairon and A. Mysyrowicz, Femtosecond filamentation in transparent media, Phys. Rep. **441**, 47 (2007); L. Bergé, S. Skupin, R. Nuter, J. Kasparian, and J.-P. Wolf, Ultrashort filaments of light in weakly ionized, optically transparent media, Rep. Prog. Phys. **70**, 1633 (2007).

[2] J. K. Wahlstrand, Y.-H. Cheng, and H. M. Milchberg, Absolute measurement of the transient optical nonlinearity in N_2, O_2, N_2O, and Ar, Phys. Rev. A **85**, 043820 (2012).

[3] V. Shumakova, S. Ališauskas, P. Malevich, C. Gollner, A. Baltuška, D. Kartashov, A. M. Zheltikov, A. V. Mitrofanov, A. A. Voronin, D. A. Sidorov-Biryukov, and A. Pugžlys,

Filamentation of mid-IR pulses in ambient air in the vicinity of molecular resonances, Opt. Lett. **43**, 2185 (2018).
[4] V. Shumakova, S. Ališauskas, P. Malevich, A. A. Voronin, A. V. Mitrofanov, D. A. Sidorov-Biryukov, A. M. Zheltikov, D. Kartashov, A. Baltuška, and A. Pugžlys, Chirp-controlled filamentation and formation of light bullets in the mid-IR, Opt. Lett. **44**, 2173 (2019).
[5] Y. E. Geints and A. A. Zemlyanov, Single and multiple filamentation of multi-terawatt CO_2-laser pulses in air: Numerical simulations, J. Opt. Soc. Am. B **31**, 788 (2014).
[6] L. Bergé, Jérémie Rolle, and Christian Köhler, Enhanced self-compression of mid-infrared laser filaments in argon, Phys. Rev. A **88**, 023816 (2013).
[7] L. Bergé, Self-compression of 2 μm laser filaments, Opt. Express **16**, 21529 (2008).
[8] P. Panagiotopoulos, P. Whalen, M. Kolesik, and J. V. Moloney, Super high power mid-infrared femtosecond light bullet, Nat. Photonics **9**, 543 (2015).
[9] P. Panagiotopoulos, P. Whalen, M. Kolesik, and J. V. Moloney, Carrier field shock formation of long-wavelength femtosecond pulses in single-crystal diamond and air, J. Opt. Soc. Am. B **32**, 1718 (2015).
[10] P. Panagiotopoulos, K. Schuh, M. Kolesik, and J. V. Moloney, Simulations of 10 μm filaments in a realistically modeled atmosphere, J. Opt. Soc. Am. B **33**, 2154 (2016).
[11] K. Schuh, M. Kolesik, E. M. Wright, J. V. Moloney, and S. W. Koch, Self-Channeling of High-Power Long-Wave Infrared Pulses in Atomic Gases, Phys. Rev. Lett. **118**, 063901 (2017).
[12] S. Tochitsky, E. Welch, M. Polyanskiy, I. Pogorelsky, P. Panagiotopoulos, M. Kolesik, E. M. Wright, S. W. Koch, J. V. Moloney, J. Pigeon, and C. Joshi, Megafilament in air formed by self-guided terawatt long-wavelength infrared laser, Nat. Photonics **13**, 41 (2019).
[13] K. Schuh, J. V. Moloney, and S. W. Koch, Interaction-induced nonlinear refractive-index reduction of gases in the midinfrared regime, Phys. Rev. E **93**, 013208 (2016).
[14] D. Woodbury, R. M. Schwartz, E. Rockafellow, J. K. Wahlstrand, and H. M. Milchberg, Absolute Measurement of Laser Ionization Yield in Atmospheric Pressure Range Gases over 14 Decades, Phys. Rev. Lett. **124**, 013201 (2020).
[15] See Supplemental Material at http://link.aps.org/supplemental/10.1103/PhysRevLett.125.133201 for calculation of the effective Rayleigh-Gans index and extinction losses, a comparison with full Mie scattering, discussion of thermal equilibration in the avalanche plasma and approximations in the temperature model, simulations of lower initial aerosol densities, and a detailed description of our UPPE implementation, which includes Refs. [16–27].
[16] E. M. Wright, S. W. Koch, M. Kolesik, and J. V. Moloney, Memory effects in the long-wave infrared avalanche ionization of gases: A review of recent progress, Rep. Prog. Phys. **82**, 064401 (2019).
[17] X. Gao and B. Shim, Impact-ionization mediated self-focusing of long-wavelength infrared pulses in gases, Opt. Lett. **44**, 827 (2019).
[18] A. W. Ali, On laser air breakdown, threshold power and laser generated channel length, Naval Research Lab Washington, DC Memorandum Report No. 5187, 1983, https://apps.dtic.mil/dtic/tr/fulltext/u2/a133211.pdf.
[19] E. Yablonovitch, Similarity principles for laser-induced breakdown in gases, Appl. Phys. Lett. **23**, 121 (1973).
[20] P. Felsenthal and J. M. Proud, Nanosecond-pulse breakdown in gases, Phys. Rev. **139**, A1796 (1965).
[21] J. D. Huba, *NRL Plasma Formulary Supported by The Office of Naval Research* (Naval Research Laboratory, Washington, DC, 2013).
[22] A. B. Langdon, Nonlinear Inverse Bremsstrahlung and Heated-Electron Distributions, Phys. Rev. Lett. **44**, 575 (1980).
[23] A. L. Milder *et al.*, Evolution of the Electron Distribution Function in the Presence of Inverse Bremsstrahlung Heating and Collisional Ionization, Phys. Rev. Lett. **124**, 025001 (2020).
[24] J. M. Liu, J. S. De Groot, J. P. Matte, T. W. Johnston, and R. P. Drake, Measurements of Inverse Bremsstrahlung Absorption and Non-Maxwellian Electron Velocity Distributions, Phys. Rev. Lett. **72**, 2717 (1994).
[25] Y. Itikawa, *Molecular Processes in Plasmas* (Springer-Verlag, Berlin, 2007).
[26] F. Brunel, Not-So-Resonant, Resonant Absorption, Phys. Rev. Lett. **59**, 52 (1987).
[27] J. P. Palastro, T. M. Antonsen, Jr., and H. M. Milchberg, Compression, spectral broadening, and collimation in multiple, femtosecond pulse filamentation in atmosphere, Phys. Rev. A **86**, 033834 (2012).
[28] R. M. Schwartz, D. Woodbury, J. Isaacs, P. Sprangle, and H. M. Milchberg, Remote detection of radioactive material using mid-IR laser-driven electron avalanche, Sci. Adv. **5**, eaav6804 (2019).
[29] D. Woodbury, R. M. Schwartz, and H. M. Milchberg, Measurement of ultralow radiation-induced charge densities using picosecond mid-IR laser-induced breakdown, Optica **6**, 811 (2019).
[30] Y. Itikawa, Cross sections for electron collisions with oxygen molecules, J. Phys. Chem. Ref. Data **38**, 1 (2009).
[31] Y. Itikawa, Cross sections for electron collisions with nitrogen molecules, J. Phys. Chem. Ref. Data **35**, 31 (2006).
[32] H. C. van de Hulst, *Light Scattering by Small Particles* (Dover, New York, 1981).
[33] K. Y. Kim, I. Alexeev, E. Parra, and H. M. Milchberg, Time-Resolved Explosion of Intense-Laser-Heated Clusters, Phys. Rev. Lett. **90**, 023401 (2003).
[34] A. V. Phelps and L. C. Pitchford, Anisotropic scattering of electrons by N_2 and its effect on electron transport, Phys. Rev. A **31**, 2932 (1985).
[35] B. C. Stuart, M. D. Feit, S. Herman, A. M. Rubenchik, B. W. Shore, and M. D. Perry, Nanosecond-to-femtosecond laser-induced breakdown in dielectrics, Phys. Rev. B **53**, 1749 (1996).
[36] N. Kroll and K. M. Watson, Theoretical study of ionization of air by intense laser pulses, Phys. Rev. A **5**, 1883 (1972).
[37] G. M. Weyl and D. Rosen, Laser-induced breakdown in argon at 0.35 μm: Theory and experiments, Phys. Rev. A **31**, 2300 (1985).
[38] J. Isaacs, C. Miao, and P. Sprangle, Remote monostatic detection of radioactive material by laser-induced breakdown, Phys. Plasmas **23**, 033507 (2016).

[39] J. Isaacs, D. Woodbury, and P. Sprangle, Remote detection of radioactive material using optically induced air breakdown ionization, Proc. SPIE Int. Soc. Opt. Eng. **11010**, 11010E (2019).

[40] J. Isaacs, The physics of high-intensity laser-matter interactions and applications, Ph.D. thesis, University of Maryland, 2019.

[41] A. W. Ali, Electron energy loss rates in N_2, O_2, and air, NRL memorandum report 5400, 1984, https://apps.dtic.mil/dtic/tr/fulltext/u2/a145158.pdf.

[42] L. Morawska, A. Afshari, G. N. Bae, G. Buonanno, C. Y. H. Chao, O. Hänninen, W. Hofmann, C. Isaxon, E. R. Jayaratne, P. Pasanen, T. Salthammer, M. Waring, and A. Wierzbicka, Indoor aerosols: From personal exposure to risk assessment, Indoor air **23**, 462 (2013).

[43] S. J. Chen, T. C. Lin, J. H. Tsai, L. T. Hsieh, and J. Y. Cho, Characteristics of indoor aerosols in college laboratories, characteristics of indoor aerosols in college laboratories, Aerosol Air Qual. Res. **13**, 649 (2013).

[44] A. F. Vette, A. W. Rea, P. A. Lawless, C. E. Rodes, G. Evans, V. R. Highsmith, and L. Sheldon, Characterization of indoor-outdoor aerosol concentration relationships during the Fresno PM exposure studies, Aerosol Sci. Technol. **34**, 118 (2001).

[45] S. Zahedpour, S. W. Hancock, and H. M. Milchberg, Ultrashort infrared 2.5–11 μm pulses: Spatiotemporal profiles and absolute nonlinear response of air constituents, Opt. Lett. **44**, 843 (2019).

[46] J. J. Pigeon, S. Y. Tochitsky, E. C. Welch, and C. Joshi, Measurements of the nonlinear refractive index of air, N_2 and O_2 at 10 μm using four-wave mixing, Opt. Lett. **41**, 3924 (2016).

[47] M. Kolesik and J. V. Moloney, Nonlinear optical pulse propagation simulation: From Maxwell's to unidirectional equations, Phys. Rev. E **70**, 036604 (2004).

[48] D. Jang, R. M. Schwartz, D. Woodbury, J. Griff-McMahon, A. H. Younis, H. M. Milchberg, and K. Y. Kim, Efficient terahertz and Brunel harmonic generation from air plasma via mid-infrared coherent control, Optica **6**, 1338 (2019).

[49] S. V. Popruzhenko, V. D. Mur, V. S. Popov, and D. Bauer, Strong Field Ionization Rate for Arbitrary Laser Frequencies, Phys. Rev. Lett. **101**, 193003 (2008).

[50] D. Arnold, E. Cartier, and D. J. DiMaria, Acoustic-phonon runaway and impact ionization by hot electrons in silicon dioxide, Phys. Rev. B **45**, 1477(R) (1992).